Characteristics of high-temperature heat-affected zones in duplex stainless steels

E. M. Westin[1] · S. Wessman[2,3]

Abstract
The level of ferritization in the high temperature heat-affected zone (HT-HAZ) affects the weldability of duplex stainless steels. The modern grades show different sensitivity and especially the nitrogen content has been proposed to control the grain growth and austenite formation. In this work, 3-, 4- and 5-mm thick UNS S32101, UNS S32304, UNS S32205 and UNS S32750 with a nitrogen range of 0.09–0.28 wt.-% were considered. Gas tungsten arc welding (GTAW) was conducted bead-on-plate with pure argon (Ar) and $Ar + 2\%\ N_2$ as shielding gas. Measurements of the HT-HAZ width and ferrite content were compared with values reported for welds and thermo-mechanical Gleeble® simulations in existing literature. The HT-HAZ width decreased with the material thickness and the nitrogen content in the base metal, while only the nitrogen alloying had a clear effect on the phase balance. Nitrogen additions to the shielding gas efficiently counteracted weld metal nitrogen loss and improved the austenite formation as compared to 100% Ar but had no clear effect on the HT-HAZ width nor ferrite content. A positive influence of the base material nitrogen content on the phase balance could be validated with thermodynamic simulations using Thermo-Calc and DICTRA, but the negative effect of high cooling rates was underestimated.

1 Introduction

The ferritic-austenitic (duplex) stainless steels combine the advantages of both ferritic and austenitic grades resulting in high strength and corrosion resistance. These alloys are typically used at temperatures from –50 °C up to max. 250 °C in a wide range of applications including the chemical, pulp & paper and oil & gas industries. The weldability of the duplex stainless steels is largely determined by the ability to form austenite and for this reason, the specifications normally require an average weld metal ferrite content of 30–70% [1]

✉ S. Wessman
sten.wessman@hv.se

1   voestalpine Böhler Welding Austria GmbH,
     Böhler-Welding-Str. 1, 8605 Kapfenberg, Austria

2   Department of Engineering Science, University West,
     46186 Trollhättan, Sweden

3   Swerim AB, Box 7047, 16407 Kista, Sweden

or 35–65% [2–5]. Significant ferritization is associated with intragranular precipitation of chromium nitrides of primarily Cr_2N type, which in turn can have a negative effect on the local corrosion resistance [6–15]. High ferrite contents in the weld metal and heat-affected zone (HAZ) have especially been reported for autogenous welding of the alloys UNS S32304, UNS S31803 and UNS S32205 [16–18].

The austenite formation, ductility and pitting resistance have been improved in modern grades by utilizing nitrogen as alloying element [19–21]. The toughness is dependent upon several factors such as the weld metal oxygen content, welding method, composition, and microstructure. Generally, very favorable results are obtained as long as the slag levels are low and reasonable fractions of austenite have formed in the weld metal and reformed in the HAZ [22]. To avoid excessive ferrite levels in the weld metal, it is generally recommended to use a filler metal that is over-alloyed in nickel [23]. In gas tungsten arc welding (GTAW), additions of 1–3% nitrogen to the argon-based shielding gas and nitrogen-based backing gas ($N_2 + 0$–10% H_2) can compensate nitrogen loss and improve the austenite formation and pitting resistance [24–30]. It is still debated if there is

a considerable loss of nitrogen also from the HAZ during normal welding conditions and if this could affect the properties further [31, 32]. Stationary arc welding bead-on-plate has shown some nitrogen loss in the high temperature HAZ (HT-HAZ) of UNS S32101, but this could not be confirmed in travelling arc welding of the same grade [33].

The HT-HAZ in duplex grades typically refers to a temperature range associated with significant grain coarsening in the single-phase ferrite region, typically exceeding 1250 °C [34]. To study the HT-HAZ in detail, thermomechanical simulations are normally required to create a sufficiently large area of uniform structure for testing [8, 9, 31–33, 35–47]. By heating samples to temperatures close to the melting point, it is possible to observe grain growth in the fully ferritic range and quantify the effect of the cooling rate on the austenite reformation and impact toughness. Various duplex stainless steels have been suggested to behave differently and be more or less susceptible to ferritization [48, 49]. The alloys UNS S32101, UNS S32304, UNS S32205 and UNS S32750 have all been reported to have a ferritic single-phase region below solidus, with the fully ferritic regions becoming narrower with higher nitrogen content [36, 39, 48, 50]. The austenite reformation has been proposed to be mainly affected by the base material nitrogen content and the cooling rate [36, 51].

The aim of the work was to evaluate the ferrite content and grain growth in the HT-HAZ of lean, standard and super duplex grades welded bead-on-plate with the GTAW process. By keeping the arc energy constant, the focus was on the effect of the material thickness and chemical composition, where the weld metal nitrogen content could be varied by using either pure argon (Ar) or Ar + 2% N_2 as shielding gas. The goal was to see if the morphology of the HT-HAZ was affected and compare the obtained results

with thermodynamic simulations, but also measurements for actual welds and thermo-mechanical simulations reported in the literature.

2 Experimental

The chemical compositions of the base materials used are presented in Table 1. Welding was performed autogenously (without filler) bead-on-plate with the GTAW process. The equipment was a modified EWM TIG 450 DC-P (EWM AG, Mündersbach, Germany) and the parameters were logged using WeldAnalyst® Version 4 (HKL Prozesstechnik, Halle, Germany). The electrode was of W-Th type with 60° sharpening angle, and it was reground between each new gas combination or as needed. The electrode stick-out was 5 mm and the arc length 2.5 mm. For the targeted arc energy of 0.4 kJ/mm, the current was set at 85 A, with the average voltage measured at 10.6 ± 0.3 V and the welding speed at 2.1 ± 0.1 mm/s.

Cross-sections of the welds were prepared using standard techniques to 3 μm and polished with SiO_2 in the last step. The microstructure was elucidated with a modified Beraha II etchant (60 ml H_2O + 30 ml HCl + 0.9–1 g $K_2S_2O_5$) and the ferrite content measured with image analysis using the software Optimas 6.1 (Media Cybernetics Inc., Rockville, Maryland, USA). The HT-HAZ was defined as the area between the fusion line and visibly affected base material, where no, or little austenite stringers remained from the original microstructure, Fig. 1. This includes the temperature range from the melting point down to approximately 1000 °C [52]. The HT-HAZ width was determined at a minimum of 10 locations. No actions were taken to specify where the low temperature HAZ (LT-HAZ) is located as this area was not part of this study. It should be noted that determining the

Table 1 Chemical composition of the base material, wt.-%

Material	Thickness, mm	C	Si	Mn	P	S	Cr	Ni	Mo	Cu	N	Cr_{eq}*	Ni_{eq}*	FN*
UNS S32101	3	0.034	0.71	4.94	0.021	0.001	21.62	1.54	0.32	0.28	0.230	21.9	7.4	> 100
UNS S32101	4	0.026	0.68	5.02	0.022	0.001	21.56	1.48	0.29	0.31	0.213	21.9	6.7	> 100
UNS S32101	5	0.035	0.73	5.04	0.017	0.001	21.56	1.52	0.30	0.32	0.220	21.9	7.2	> 100
UNS S32304	3	0.018	0.42	1.52	0.022	0.001	22.76	4.83	0.29	0.26	0.096	23.1	7.4	> 100
UNS S32304	4	0.016	0.37	1.47	0.022	0.001	22.82	4.80	0.42	0.25	0.090	23.2	7.3	> 100
UNS S32304	5	0.018	0.46	1.53	0.027	0.001	22.81	4.73	0.28	0.26	0.093	23.1	7.3	> 100
UNS S32205	3	0.013	0.40	1.48	0.020	0.001	22.36	5.75	3.21	0.12	0.188	25.6	10.0	87.0
UNS S32205	4	0.015	0.40	1.49	0.021	0.001	22.56	5.63	3.18	0.15	0.172	25.7	9.6	96.0
UNS S32205	5	0.016	0.39	1.43	0.022	0.001	22.39	5.70	3.19	0.20	0.178	25.6	9.9	89.4
UNS S32750	3	0.014	0.20	0.77	0.024	0.001	24.72	6.78	3.77	0.19	0.256	28.5	12.4	75.9
UNS S32750	4	0.013	0.23	0.82	0.018	0.001	24.90	6.94	3.81	0.18	0.271	28.7	12.9	72.3
UNS S32750	5	0.015	0.22	0.69	0.022	0.001	25.04	6.95	3.82	0.25	0.280	28.9	13.1	70.3

*Calculated using the WRC'92 diagram
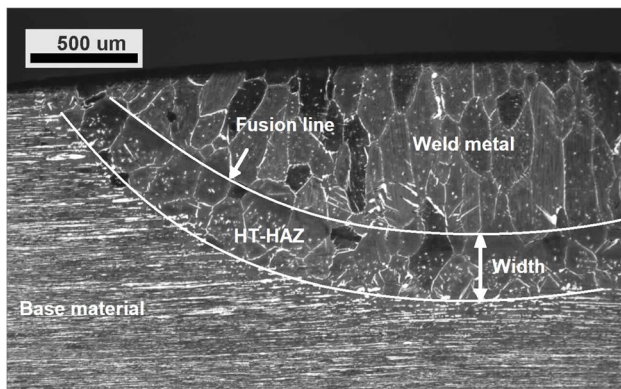
Fig. 1 HT-HAZ with visual grain growth (5 mm UNS 32304 welded with Ar)

Fig. 2 Fusion line in 5 mm **a** UNS S32205 (Ar + 2% N_2) and **b** UNS S32304 (100% Ar)

precise location of the fusion line posed a challenge for all materials. This is a recognized phenomenon, particularly pronounced for duplex alloys with high austenite reformation capacity [53]. Several samples had to be prepared anew and while still using Beraha II as etchant, the final polishing step and etching time were modified. The aim was to either enhance the dendritic substructure (seen as relief structures in highly ferritic welds) in the weld metal or intentionally induce selective blur to be able to distinguish the weld metal from the HT-HAZ. The difference in chemical composition and ferrite content yielded different etching responses. Electropolishing proved, for instance, beneficial for the materials alloyed with molybdenum (UNS S32205 and UNS S32750), enhancing the regions with chromium nitrides in the HT-HAZ, Fig. 2a. However, these deliberate alterations compromised the surface quality rendering it unsuitable for image analysis. Light settings and focus depth in the light optical microscope (LOM) were also adjusted to accentuate the dendritic structure, exclusively present in the fused weld metal, Fig. 2b.

Calculations of the fraction of equilibrium phases as a function of temperature and thereby the fully ferritic region were performed using the CALPHAD (calculation of phase diagrams) based [54] software Thermo-Calc version 2022a (Thermo-Calc Software AB, Solna, Sweden) with the database TCFE11 for thermodynamics. Laves, π and R phase were omitted. These may precipitate in duplex alloys on equilibrium, but for the short times experienced in bead-on-plate welding and HT-HAZ simulation, no precipitates of these types have been reported in the literature. Eta η nitride reported for super austenitics [55] was for the same reason also omitted.

To be able to simulate the influence of a given cooling rate on microstructure development, it was necessary to consider diffusion-controlled reactions. Mobility calculations were conducted using the diffusion module
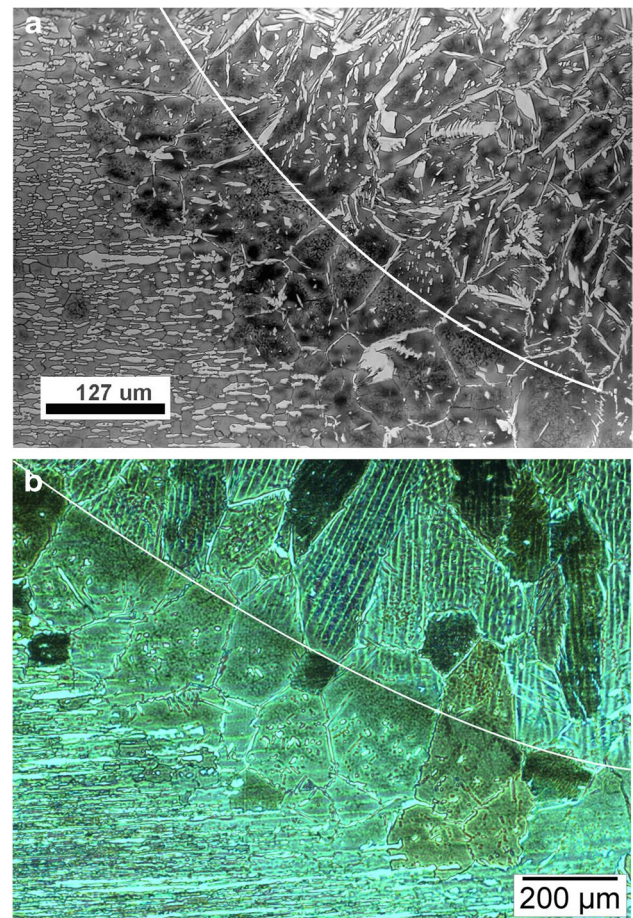
DICTRA (diffusion-controlled transformation) within the Thermo-Calc package. In addition to the TCFE11 database for thermodynamics, a mobility database was essential for the coefficients in the diffusion equations. In this case, the MOBEFE7 database was utilized as a supplement. 1D kinetic simulation was applied assuming planar growth, a system cell size of 10 μm, and cooling rates of 20 °C/s (air cooling), 75 °C/s (intermediate cooling) and 400 °C/s (water quenching) [33]. Ferrite was selected as active phase with 100 vol.-% at the start where the austenite was inactive, precipitating and growing when stable. The cooling was simulated for a range from 1600 °C to 1000 °C to include solidification and all temperatures relevant for the austenite formation [52]. Although the paper focuses on the HT-HAZ, the weld metal is also relevant due to potential nitrogen loss through diffusion from the HT-HAZ to the melt. To isolate the effect of nitrogen and circumvent the inability of the system to handle all elements, the chemical compositions were simplified, Table 2. The lowest nitrogen content was set to 0.01 wt.-% as 0 wt.-% may cause numerical problems.

Table 2 Compositions used for the simplification of the mobility simulations studying the ferrite content as a function of the cooling rate and nitrogen loss, wt.-%

Material	Cr	Ni	Mo	Mn	Original nitrogen content*	50% nitrogen loss	Complete nitrogen loss
UNS S32101	21.0	1.5	0.3	5.0	0.22	0.11	0.01
UNS S32304	23.0	4.8	0.3	1.5	0.10	0.05	0.01
UNS S32205	22.0	5.5	3.0	1.5	0.18	0.09	0.01
UNS S32750	25.0	7.0	4.0	0.8	0.27	0.13	0.01

*Nitrogen content in the unaffected (as-delivered) base material

3 Results and discussion

3.1 Bead-on-plate welds

Figure 3 shows the appearance of the welds on the 3 mm thick material. Some samples had somewhat rounded edges from the sample preparation. The weld metal austenite formation increased for all welds performed with Ar + 2% N_2 as compared to Ar and an austenite layer formed on the weld metal and HT-HAZ. With Ar, the austenite layer was only located on the base material. This is of importance as it can lead to exposure of large ferrite grains with Cr_2N to the corrosive medium and in turn result in lower resistance to local corrosion [56, 57].

The measurements of ferrite, weld shape and HAZ width are shown in Table 3. The weld metal width, depth and reinforcement could not be correlated with the base material thickness nor alloy type. With nitrogen additions to the shielding gas, the weld width increased somewhat, but no clear effect on the depth and reinforcement could be confirmed. The weld penetration is well-known to be affected by the composition of the base material (including residuals and micro-alloying elements) and there can be a substantial variation from heat to heat [58]. Especially the elements sulfur and oxygen would have a positive effect affecting the Marangoni flow, and nitrogen be negative. [33]. The latter two could also be introduced through the shielding gas.

The width of the HAZ decreased with the base material thickness and the nitrogen content for all base materials, Fig. 4a. The widest HAZ and highest ferrite contents were, as expected, observed for the UNS S32304 welds [36, 49]. The austenite reformation was on average higher with higher alloy nitrogen content, but no clear relationship could be seen with the thickness, Fig. 4b. For the HAZ, the shielding gas composition had no measurable influence on the width nor ferrite content.

Additionally, the formation of austenite in the weld metal increased with both the base material nitrogen content and addition of nitrogen to the shielding gas, Fig. 5a. When using Ar, nitrogen loss occurred from the weld metal and the ferrite content was often higher than in the HT-HAZ.

On the contrary, the use of Ar + 2% N_2 consistently resulted in higher austenite formation in the weld metal. This difference was particularly pronounced for UNS S32304. In the HT-HAZ, the reformation of austenite also increased with higher nitrogen alloying content, as illustrated in Fig. 5b. However, no further improvement could be seen with nitrogen additions to the shielding gas. The shielding gas thus had limited influence on the ferrite content in the HT-HAZ, aligning with earlier findings in GTAW [31, 33] and laser welding [59].

None of the welds in any of the base materials showed a ferrite content below the most stringent limit 65 vol.-% and only the 3 mm UNS S32750 weld performed with Ar + 2% N_2 was below 70 vol.-% ferrite in both the weld metal and HAZ. The low austenite formation can be explained by the rapid cooling caused by welding at fairly low arc energy (0.4 kJ/mm) and bead-on-plate as compared to full penetration welding. This means that additions of filler metal are necessary to achieve the 35–65 vol.-% requirement in the weld metal and that the requirements may not at all be achievable in the HT-HAZ. The maximum penetration depth measured for the 3-, 4- and 5 mm thick sheets was only 1/3, 1/4 and 1/5 of the material thickness, respectively. By proper joint preparation, the cooling rate would be reduced, and subsequent welds partly reheat the HAZ of previous weld beads [60, 61]. However, this work only takes single bead welding into consideration and therefore no austenite growth and formation of secondary austenite in the HAZ.

When measuring the ferrite content of the HAZ, a magnification of 1000× was used to ensure that not any base material was included. Corolleur et al. [17] debated that the use of 1000× magnification for determination of the ferrite content in the HAZ mainly measures the ferrite content in the HT-HAZ, which may be too conservative. As the HT-HAZ of UNS S32304 in their work was nearly fully ferritic, high magnification would make it virtually impossible to pass the 35–65 vol.-% ferrite requirement. A similar conclusion was drawn by Yasuda et al. [62] who conducted HT-HAZ simulations of UNS S31803 at 1350 °C and reported that it was not possible to reach 40 vol.-% austenite even at very low cooling rates.

Fig. 3 Etched cross-section of 3 mm thick material welded with Ar or Ar + 2% N₂ as shielding gas (different scales)
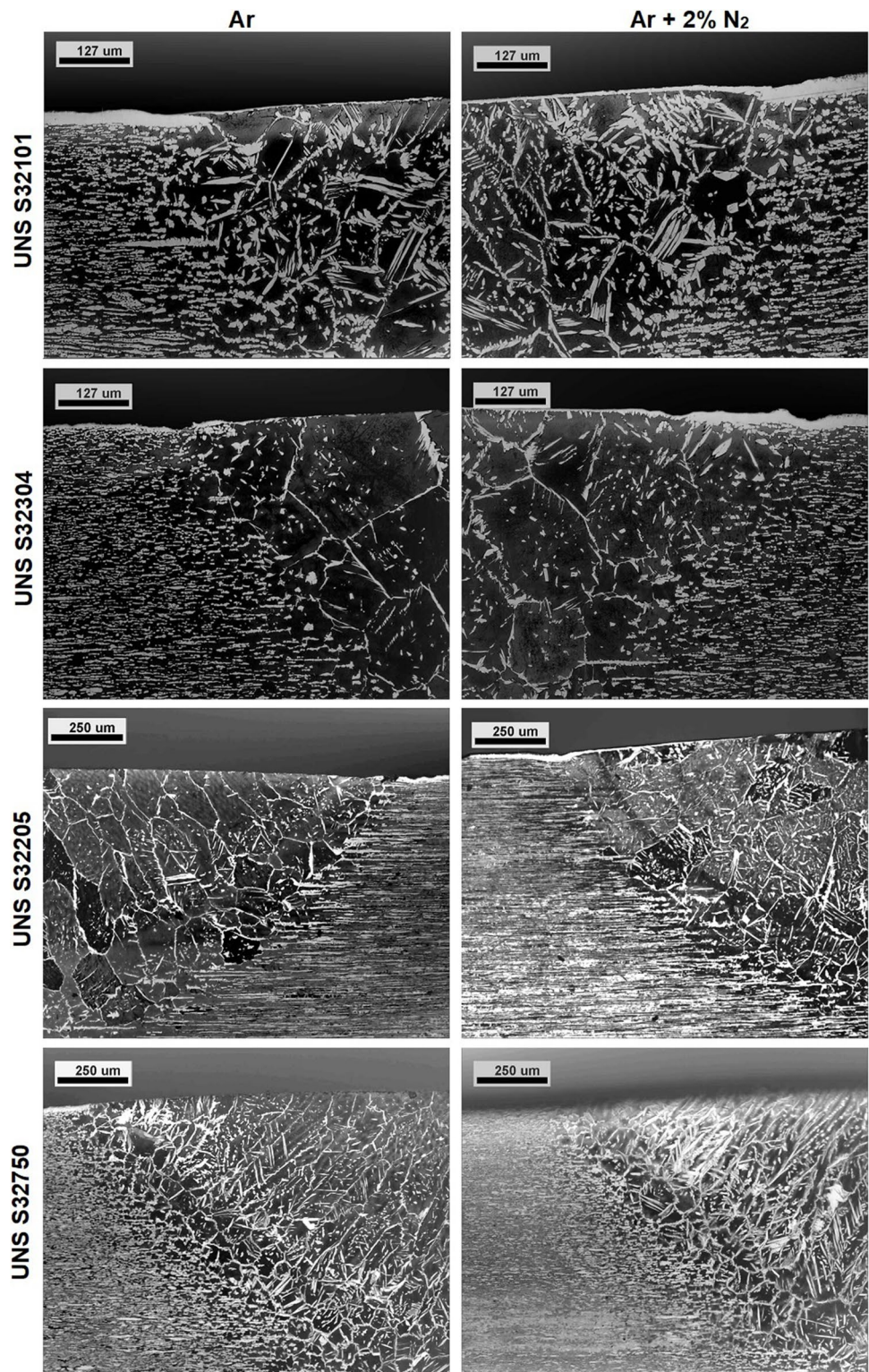
3.2 Expected effects on the HT-HAZ properties

It is well known that the impact toughness and the local corrosion resistance of the HT-HAZ are somewhat lower due to grain growth, ferritization and formation of Cr_2N precipitates [8, 63, 64]. Due to the peak temperature gradients, the HAZ is not a uniform structure and the actual effect on a welded joint is not so easy to determine [37]. In case of multipass welding, subsequent passes also cause reheating [65, 66]. Corrosion testing as per ASTM G48 Method A [67]. ASTM A923

Table 3 HAZ width and ferrite content measured for bead-on-plate welds

Material	Thickness, mm	Shielding gas	HAZ width, μm	Ferrite content, vol.-%		Weld shape, mm		
				Weld metal	HAZ	Width	Depth	Reinforcement
UNS S32101	3	Ar	248 ± 58	78 ± 3	74 ± 6	3.83	0.95	0.08
UNS S32101	3	Ar + 2% N$_2$	214 ± 36	70 ± 2	70 ± 4	4.03	0.80	0.11
UNS S32101	4	Ar	200 ± 11	79 ± 5	69 ± 2	3.89	1.04	0.08
UNS S32101	4	Ar + 2% N$_2$	201 ± 19	72 ± 3	73 ± 1	4.12	1.08	0.11
UNS S32101	5	Ar	162 ± 36	84 ± 1	82 ± 3	3.43	0.87	0.08
UNS S32101	5	Ar + 2% N$_2$	174 ± 29	70 ± 3	75 ± 1	3.78	0.71	0.11
UNS S32304	3	Ar	314 ± 10	93 ± 1	91 ± 3	3.54	0.87	0.11
UNS S32304	3	Ar + 2% N$_2$	365 ± 30	78 ± 1	91 ± 1	3.62	0.81	0.08
UNS S32304	4	Ar	310 ± 27	95 ± 1	90 ± 1	3.84	0.86	0.12
UNS S32304	4	Ar + 2% N$_2$	318 ± 28	74 ± 3	92 ± 2	3.77	0.71	0.11
UNS S32304	5	Ar	282 ± 45	89 ± 4	89 ± 2	4.09	0.81	0.08
UNS S32304	5	Ar + 2% N$_2$	269 ± 22	81 ± 3	90 ± 2	4.38	0.81	0.08
UNS S32205	3	Ar	263 ± 38	83 ± 1	85 ± 1	4.34	1.22	0.10
UNS S32205	3	Ar + 2% N$_2$	243 ± 47	75 ± 1	80 ± 1	4.68	1.23	0.10
UNS S32205	4	Ar	221 ± 14	88 ± 1	89 ± 1	3.65	0.79	0.11
UNS S32205	4	Ar + 2% N$_2$	220 ± 16	77 ± 1	91 ± 2	4.02	0.95	0.11
UNS S32205	5	Ar	153 ± 10	83 ± 6	86 ± 3	3.07	0.73	0.11
UNS S32205	5	Ar + 2% N$_2$	154 ± 29	82 ± 4	86 ± 3	3.89	1.06	0.11
UNS S32750	3	Ar	209 ± 32	77 ± 4	71 ± 5	4.09	1.00	0.08
UNS S32750	3	Ar + 2% N$_2$	220 ± 32	66 ± 7	65 ± 7	4.81	1.20	0.08
UNS S32750	4	Ar	181 ± 21	86 ± 3	82 ± 2	4.09	0.77	0.10
UNS S32750	4	Ar + 2% N$_2$	178 ± 20	77 ± 3	81 ± 2	4.71	0.88	0.12
UNS S32750	5	Ar	122 ± 14	83 ± 4	78 ± 2	4.09	0.88	0.08
UNS S32750	5	Ar + 2% N$_2$	122 ± 28	74 ± 2	76 ± 4	4.51	0.74	0.08

Method C [68] and ISO 17781 [69], where cross-sections of the welds and hence ferrite grains with Cr$_2$N precipitates are exposed to the corrosive medium, often shows that the HT-HAZ is most susceptible to pitting attack [7, 12, 70–76]. This has also been seen on welded material surfaces with ASTM G150 [77] using the so-called Avesta Cell [78, 79] if the top surfaces of the welds, cross-sections or HT-HAZ simulated samples are ground flat prior to testing and polished cross-sections [56, 57, 62, 80–82]. When the surface is instead left in as-welded condition and the root or cap tested by means of ASTM G150, only the surface exposed to the corrosive medium is taken into account. As long as filler metal has been added, the pitting attack is normally located some millimeters from the fusion line where the lowest Cr/(Cr + Fe) fraction of the oxide is found [83–86]. This coincides with the region located mostly 1–3 mm from the fusion line exposed to 500–700 °C [29, 70, 81, 82, 85, 87–89]. In this temperature range, iron diffuses faster than chromium and the resulting weld oxide becomes iron-rich with lower resistance to pitting than the chromium-rich oxide present at the surface closer to the fusion line. This zone consequently does not match that of the HT-HAZ formed at higher temperatures.

3.3 Comparison of thermo-mechanical data from HT-HAZ simulations

The grain growth and austenite reformation in the HT-HAZ have previously been investigated for the lean duplex grade UNS S32101, where thermo-mechanical Gleeble® simulations were concluded to correlate reasonably well with bead-on-plate welding [33]. The study showed that while the width of the HAZ expanded with higher heat input, the austenite reformation remained unaltered for an arc energy range of 0.4–1.2 kJ/mm. To ensure consistency within the broader scope of this work involving three other alloys, the decision was made to adopt the lowest recommended arc energy for UNS S32101, i.e., 0.4 kJ/mm. Such a low arc energy could prove beneficial, for example, in enhancing control of the melt when the process is performed manually. In practice, it is particularly applied when autogenously welding duplex alloys of up to 2 mm thickness. A typical application would be continuous welding in tubular mills. Full penetration can be achieved with a heat input of 0.12–0.14 kJ/mm in mechanized GTAW of 1 mm thick UNS S32101, UNS S32304, UNS S32205 and UNS S32750 [29].
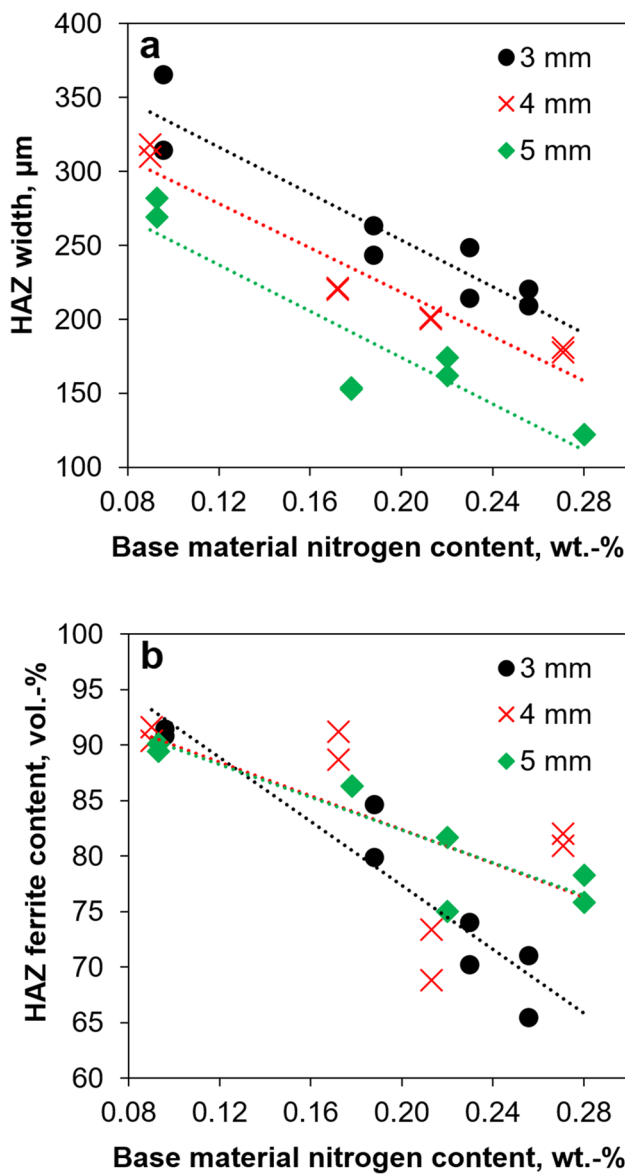
Fig. 4 HAZ **a** width and **b** ferrite content as a function of the base material nitrogen content

Fig. 5 Effect of nitrogen additions to the shielding gas on the ferrite content in the **a** weld metal and **b** HT-HAZ

As the HAZ influences the general weldability of duplex stainless steels, thermo-mechanical simulations have been performed for many alloys. Due to different methodologies, simulation parameters and means of measurement, it may not be possible to compare all results. Nevertheless, by combining data from published simulations on the same grades as in this work [16, 22, 31–33, 36, 37, 43, 44, 49], some general observations can be made, Fig. 6.

The austenite formation increases with more nitrogen in the base metal and slower cooling, Fig. 6a. The ferrite content in the simulated HT-HAZ is mostly higher than 65 vol.-% for the samples with a cooling rate relevant for welding conditions (rapid and intermediate cooling). With
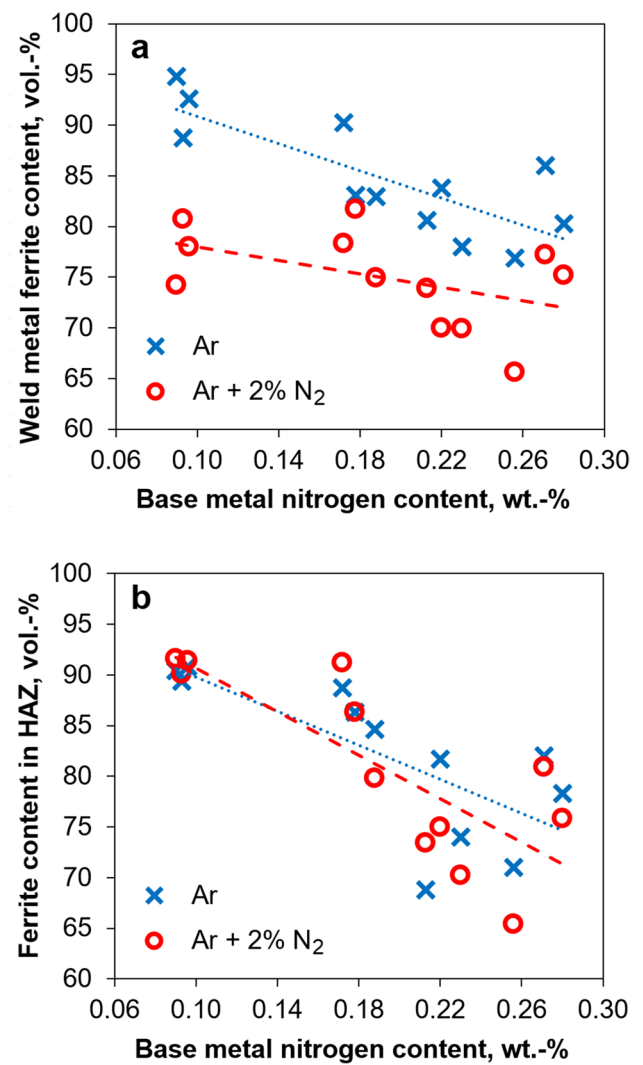
cooling in air or stepwise cooling by programming, more austenite can form, but these circumstances would rarely be found in practical welding.

Focusing solely on shorter holding times (0–5 s) at peak temperatures, a pattern emerges where the grain size becomes smaller with more nitrogen in the base material and faster cooling, Fig. 6b. In cases of slow cooling, the scatter was too large to properly see a trend. The thickness of the simulated plates was 6–15 mm and the difference in lamellar distance would affect the final grain size. The ferritization is also highly dependent on the simulation method and maximum temperature that is actually reached. For instance, the peak temperatures selected for UNS S32205 and UNS S31803 ranged from 1345 °C to 1360 °C. The impact toughness at room temperature exhibits a positive correlation with nitrogen content and slower cooling, Fig. 6c. Also here, the scatter may be due to variations in the material thickness,
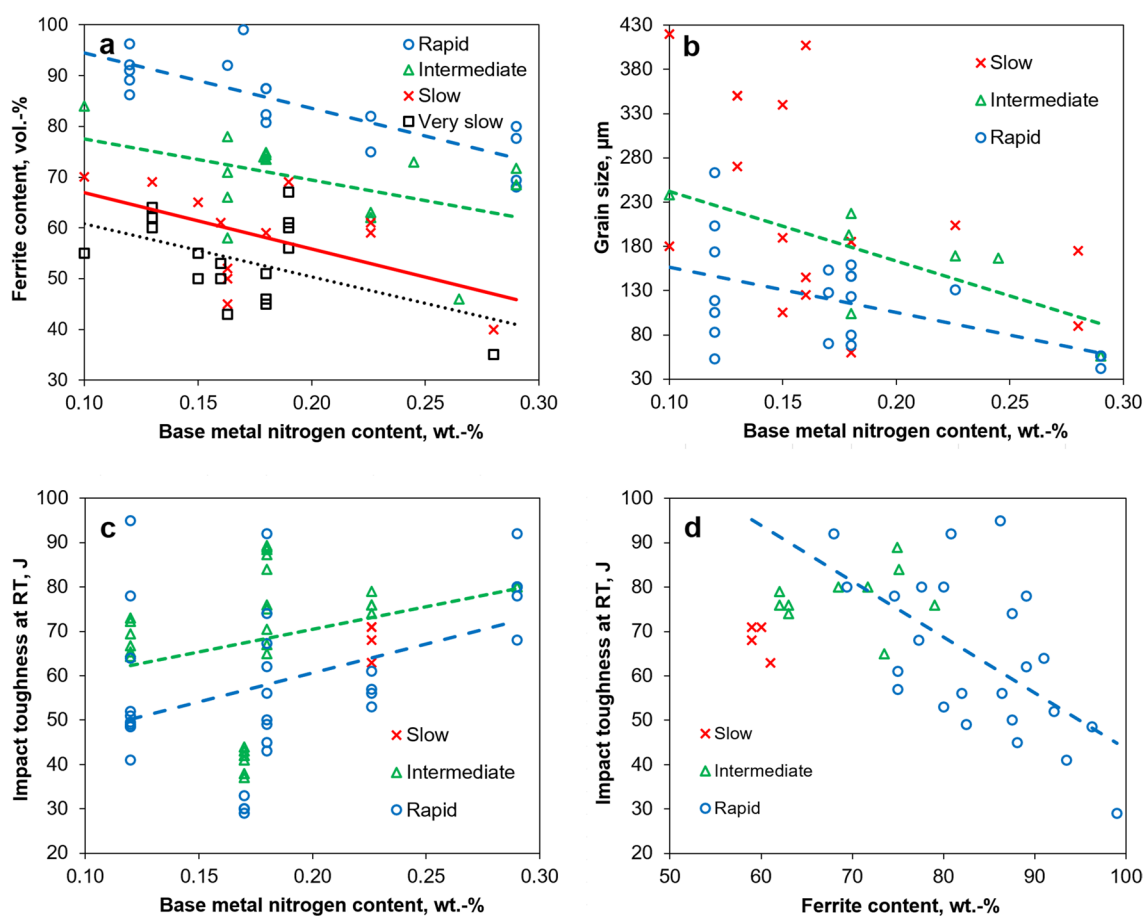
Fig. 6 Combined data from several publications on HT-HAZ simulation of different duplex stainless steels [16, 22, 31, 32, 36, 37, 43, 44, 49]. Effect of base metal nitrogen content on **a** ferrite, **b** grain size, **c** impact toughness and **d** effect of ferrite content on impact toughness at different cooling rates. The cooling rate was defined as rapid (> 400 °C/s), intermediate (80–300 °C/s), slow (15–50 °C/s) and

very slow (0–10 °C/s). Although the ferritization primarily occurs at temperatures higher than 1250 °C, the cooling time from 1200 °C to 800 °C, $t_{12/8}$, or the cooling time from 900 °C to 500 °C, $t_{9/5}$, are sometimes used to correlate the ferrite/austenite balance in the HT-HAZ [2]. Here such values were converted to cooling rate in °C/s for comparison

peak temperature and grain size, where thicker plates typically exhibit lower toughness. However, when the grain size has been varied through longer holding times at peak temperature, the effect on the impact toughness was low [22, 36, 39, 44]. The impact toughness could also be dependent on the phase balance for the rapid cooling, Fig. 6d, indicating that the high ferrite content has an influence. For the slow and intermediate cooling rates, no correlation could be seen between impact toughness and ferrite content. These findings align with the observations made by Cao and Hertzman [22], who stated that very favorable results are generally obtained when reasonable fractions of austenite have reformed in the HAZ.

Hertzman et al. [36] performed HT-HAZ simulations of different duplex stainless steels and concluded that the nitrogen diffusion controls the phase transformation rate. UNS S32304 showed the largest grain growth and lowest austenite reforming ability, and this was correlated to the

low nitrogen content (0.12 wt.-%). UNS S32205 with somewhat more nitrogen (0.18 wt.-%) showed slightly improved austenite formation, while UNS S32750 with the highest nitrogen content (0.29 wt.-%) displayed limited grain growth and the fastest austenite reformation at high cooling rates. The higher ferritization with lower nitrogen content would be an effect of a larger fully ferritic region.

For the HAZ width, the same effect of the nitrogen content could be found also in the present work, but for the ferrite content, the 3 mm thick plate showed the clearest correlation with the base material nitrogen content. For the thicker materials, the cooling rate probably became more dominant given that over 75% of the material thickness remained below the weld. In the thermo-mechanical simulations, the whole sample thickness is heated, which diminishes the temperature gradient effect. In addition, the composition and especially the nitrogen content varied between the different thicknesses as these originated from different heats.
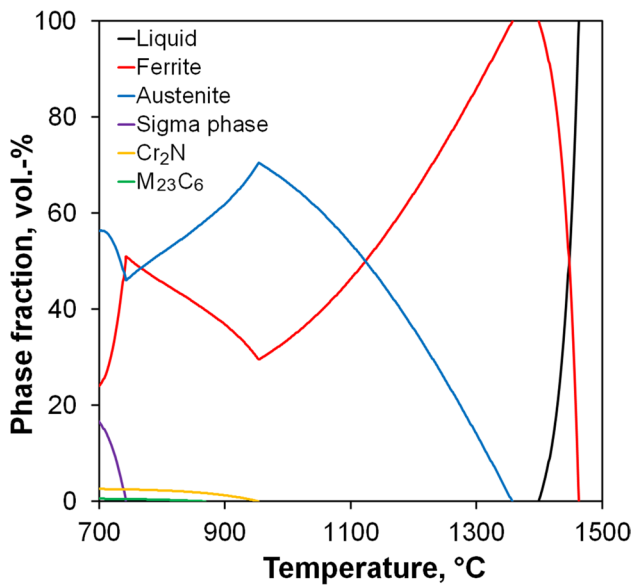
Fig. 7 Phase diagram calculated using TCFE11 for 3 mm UNS S32101

The UNS S32101 in this work showed 69–82 vol.-% ferrite in the HAZ of the bead-on-plate welds. This aligns reasonably well with the 72–87 vol.-% found for bead-on-plate welds of 6 mm material [33]. Similarly, Gleeble® HT-HAZ simulations of the same 6 mm thick plate with rapid cooling resulted in 75–82 vol.-%. Assuming that the HAZ consists of an average of 1.5 grains, the average grain size in the thermo-mechanical simulations with 0–5 s holding time was 131–194 μm for the rapid cooling and 169–214 μm for the intermediate cooling. This matches the 162–248 μm range measured with 0.4 kJ/mm heat input for the 3-, 4- and 5-mm material in this study, and 172–196 μm with 0.4 kJ/mm on 6 mm material in previous research [33].

UNS S32304 showed the lowest austenite reformation in the HAZ of all materials with approximately 90 vol.-% of ferrite. Rodriguez et al. [90] measured 77–82 vol.-% in the HAZ for the same grade of 3 mm thickness welded with a heat input range of 0.6–1.1 kJ/mm. Soares da Fonseca et al. [91] reported 78–88 vol.-% for 8 mm material welded with 0.5–3.2 kJ/mm. The higher arc energy and multipass welding would, however, affect the austenite formation. The measured HAZ width was on average 269–365 μm, which was up to twice as wide as what was estimated for UNS S32750. Corolleur et al. [17] also determined the HAZ of UNS S32304 with 0.12 wt.-% nitrogen to be fairly wide with 350 μm.

For UNS S32205, the HAZ width was 153–263 μm and the ferrite content in the HAZ was 81–90 vol.-%. As the width of the HAZ is in the range 1–2 grain diameters, this fits fairly well with the thermo-mechanical simulations in Fig. 6b. The austenite reformation was similar to the reported values for rapid cooling in Fig. 6a. For 8 mm thick UNS S32205, Soares da Fonseca et al. [91] measured 75 vol.-% for a heat input of 0.5 kJ/mm. In flux-cored arc welding of 16 mm UNS S32205 with 0.6–2.1 kJ/mm, the ferrite content in the HAZ was determined to be 61–67 vol.-% [92]. The higher heat input may allow for more austenite reformation in the HT-HAZ, but multipass welding has also been suggested to contribute by reheating [91].

For 2 mm UNS S32750, Rodriguez et al. [90] reported 45–53 vol.-% ferrite in the HAZ, which was considerably lower than the 65–71 vol.-% measured here for 3 mm material. In thermo-mechanical simulations, values around 50 vol.-% have been presented, Fig. 6a, but for rapid and intermediate cooling, most values were higher than 70 vol.-%. For 8 mm UNS S32750, Soares da Fonseca et al. [91] measured 78 vol.-% for a heat input of 0.5 kJ/mm as compared to the 86 vol.-% measured

Table 4 Temperatures calculated using TCFE11, °C. With the exception of the fully ferritic temperature range, these indicate the temperature at which formation starts

Material	Thickness, mm	Chi	Sigma	Cr$_2$N	50% austenite	Austenite	Fully ferritic range*	Solidus	Liquidus
UNS S32101	3	-	743	954	1126	1357	42	1399	1463
UNS S32101	4	-	745	945	1103	1342	67	1409	1465
UNS S32101	5	-	743	951	1121	1353	46	1399	1462
UNS S32304	3	-	798	851	1090	1288	153	1441	1476
UNS S32304	4	-	808	846	1067	1276	169	1445	1478
UNS S32304	5	-	794	854	1077	1282	160	1442	1477
UNS S32205	3	775	977	942	1117	1318	109	1427	1472
UNS S32205	4	765	972	939	1089	1306	116	1422	1474
UNS S32205	5	773	975	936	1110	1316	103	1418	1472
UNS S32750	3	777	1037	965	1126	1334	66	1401	1469
UNS S32750	4	773	1041	973	1138	1340	56	1396	1467
UNS S32750	5	775	1044	977	1147	1346	44	1390	1466

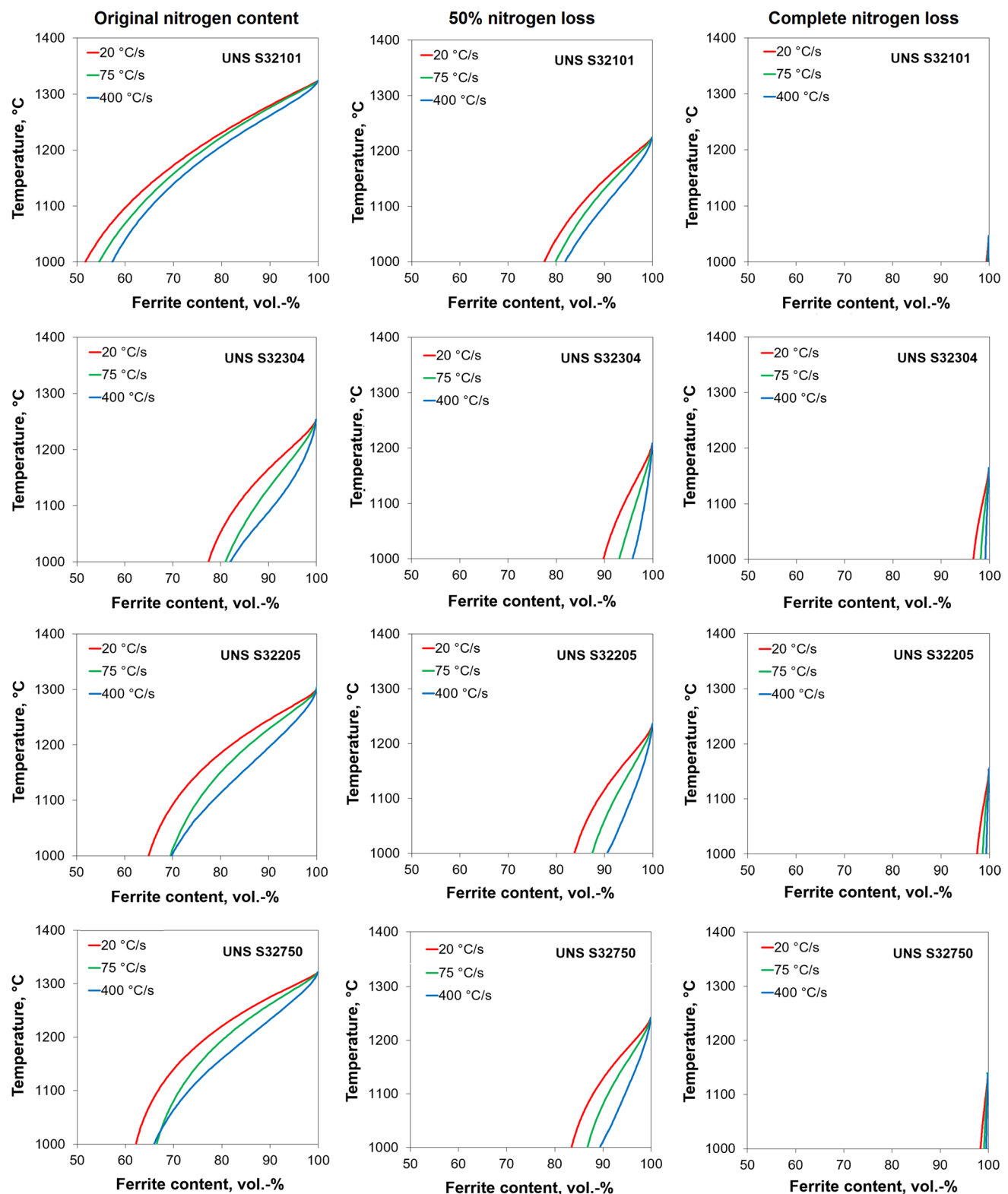* Fully ferritic range, $\Delta T = T_{solidus} - T_{ferrite\ solvus}$

Fig. 8 DICTRA simulated start temperature for austenite formation vs. ferrite fraction as a function of the nitrogen content

here for 5 mm material with 0.4 kJ/mm. The width of the HAZ of the 3–5 mm UNS S32750 in the present work was 122–220 μm, which matches the 120–130 μm found

for 5.5 mm UNS S32750 welded with 0.54 kJ/mm and 138–145 μm with 1.1 kJ/mm [93], and multipass welding of 8 mm UNS S32750 [15].

Table 5 Simulated ferrite content at 1000 °C as a function of the cooling rate and nitrogen loss using DICTRA, vol.-%

Material	Cooling rate, °C/s	Original nitrogen content*	50% nitrogen loss	Complete nitrogen loss
UNS S32101	20	51.7	77.5	99.4
UNS S32101	75	54.6	79.9	99.7
UNS S32101	400	57.3	81.9	99.8
UNS S32304	20	77.4	89.8	96.7
UNS S32304	75	80.9	93.0	98.2
UNS S32304	400	82.0	95.8	99.2
UNS S32205	20	65.0	83.8	97.4
UNS S32205	75	69.5	87.5	98.6
UNS S32205	400	69.7	90.5	99.4
UNS S32750	20	62.2	83.5	98.4
UNS S32750	75	66.5	86.7	99.1
UNS S32750	400	65.6	88.4	99.6

*Nitrogen content in the unaffected (as-delivered) base material

3.4 Thermodynamic simulations

An example of the phase diagrams calculated with TCFE11 using chemical composition for 3 mm UNS S32101 is shown in Fig. 7. The key data from the Thermo-Calc simulation at equilibrium are summarized in Table 4. The formation of sigma phase starts earlier with higher chromium and molybdenum contents (UNS S32750 → UNS S32205 → UNS S32304 → UNS S32101), while chi phase only would precipitate in the alloys containing molybdenum (UNS S32205 and UNS S32750). Neither sigma nor chi phase were detected in the welds or HAZs in this study. The calculations take into consideration equilibrium conditions, and the formation of these phases does need considerably longer duration at these temperatures than what can be achieved in the single-pass welding bead-on-plate [46].

The Thermo-Calc simulation at equilibrium would predict the fully ferritic region, $\Delta T = T_{solidus} - T_{ferrite\ solvus}$, to decease and the austenite formation rate capacity to increase with UNS S32304 → UNS S32205 → UNS S32101 ≈ UNS S32750. In the weld metal, the measured austenite formation also increased following the same ranking. Due to difficulties accurately determining the exact location of the fusion line for the alloys with high austenite content, the values for UNS S32101 and UNS S32750 are more uncertain. Nevertheless, the measured HAZ width follows the order of UNS S32304 → UNS S32205 → UNS S32101 → UNS S32750, aligning with previous findings [48]. Although UNS S32101 and UNS S32750 exhibited very similar predicted solidus and austenite formation start temperatures, this contradicted actual measurements where UNS S32750 displayed greater resistance to ferritization [48]. However, the positive effect

Table 6 Simulated austenite start temperature as a function of base material nitrogen content using DICTRA, °C

Material	Original nitrogen content*	50% nitrogen loss	Complete nitrogen loss
UNS S32101	1324	1224	1046
UNS S32304	1254	1209	1164
UNS S32205	1299	1234	1153
UNS S32750	1322	1242	1139

*Nitrogen content in the unaffected (as-delivered) base material

of nitrogen compared to UNS S32205 and especially UNS S32304 could clearly be visualized.

The Thermo-Calc simulations using DICTRA for mobilities for austenite formation are visualized in Fig. 8 and summarized in Table 5 and 6.

The DICTRA simulation predicted an austenite reformation ability of UNS S32101 → UNS S32750 → UNS S32205 → UNS S32304 and thus showed the same ranking as at equilibrium. With the original base material nitrogen content, DICTRA overestimated the austenite fraction: The simulated ferrite content would be 52–57 vol.-% for UNS S32101, 77–82 vol.-% for UNS S32304, 65–70 vol.-% for UNS S32205 and 62–66 vol.-% for UNS S32750. This is clearly lower than what was seen in the HT-HAZ of the welds performed bead-on-plate, where the measured ferrite content was 69–82 vol.-% for UNS S32101, 89–92 vol.-% for UNS S32304, 80–91 vol.-% for UNS S32205 and 65–82 vol.-% for UNS S32750. For UNS S32304 and UNS S32205, the actual values were closer to the results obtained for the simulations assuming that only 50% of the base metal nitrogen content remained. For UNS S32101 and UNS S32750, the measurements would match the simulations after a loss of approximately 25% of the nitrogen. Bead-on-plate welds performed on UNS S32101 indicate that such a considerable nitrogen loss in the HT-HAZ would not be expected [33].

For the weld metal, the austenite formation for all alloys with Ar and Ar + 2% N_2 corresponded to that of 50% and 25% nitrogen loss, respectively. In the previous work where 6 mm UNS S32101 was welded with 0.4 kJ/mm, the nitrogen loss from the weld metal with Ar was 25–35% and with Ar + 2% N_2 10–15% [33].

The start temperature for austenite formation in the DICTRA simulation decreased when the nitrogen content decreased but was independent of the cooling rate. The largest drop after complete depletion of nitrogen could be found for UNS S32101 (278 °C) followed by UNS S32750 (183 °C). These materials had the highest base material nitrogen contents with 0.22 and 0.27 wt.-%, respectively. The austenite start formation temperature for UNS S32304 only dropped 90 °C and was the highest of all materials after
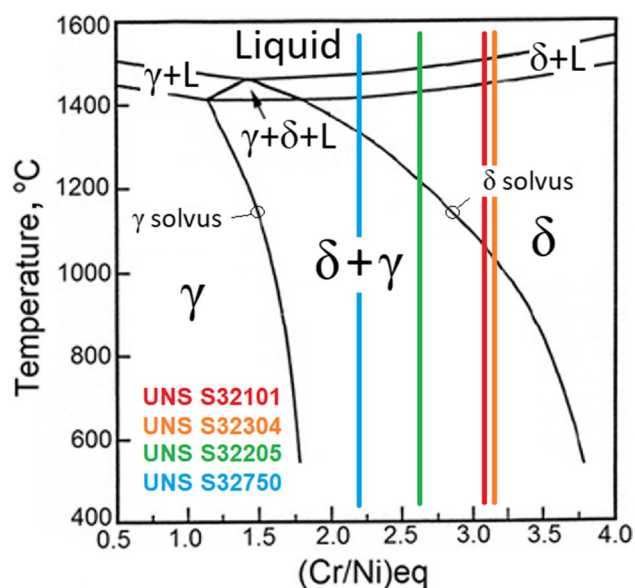
Fig. 9 Fe–Ni–Cr pseudo-binary phase diagram based on the $(Cr/Ni)_{eq}$ ratio

complete nitrogen loss. The simulation thus indicates that the alloy UNS S32304 with the lowest nitrogen solubility (0.10 wt.-%) would be less sensitive to nitrogen loss than UNS S32101. However, this could not be confirmed in the actual weld metal, where UNS S32304 showed the largest decrease in weld metal austenite content formation when welding with Ar as shielding gas, Fig. 5a.

The effect of the cooling rate was underestimated with DICTRA as compared to what has been reported for simulated HT-HAZ in the literature [16, 31, 32, 36, 37, 43, 49]. The difference in ferrite content at 1000 °C between the lowest and fastest cooling rates (20 °C/s to 400 °C/s), was predicted to be less than 7 vol.-% for all alloys, while more than 15 vol.-% has been reported for UNS S32101 [33], 21 vol.-% for UNS S32304 [36], 26 vol.-% for UNS S32205 [31] and 12 vol.-% for UNS S32750 [36].

The thermal simulation tools used here were unable to exactly predict the austenite formation temperatures of duplex stainless steel weldments. Although the trend was mostly accurate with Thermo-Calc, the rapid heating and cooling deviate from the equilibrium conditions being assumed. This calculation tool did not correctly predict the effect of the cooling rate and the susceptibility to nitrogen loss. A challenge for DICTRA is that it is not possible to include all relevant elements for austenite formation due to simulation complexity. The consequence of more components are substantially longer simulation times, possibly still not improving the results. It should also be noticed that the set-up was planar growth ferrite to austenite, omitting liquid and any secondary phases. Nevertheless, thermal simulation gives an indication of how duplex materials act upon
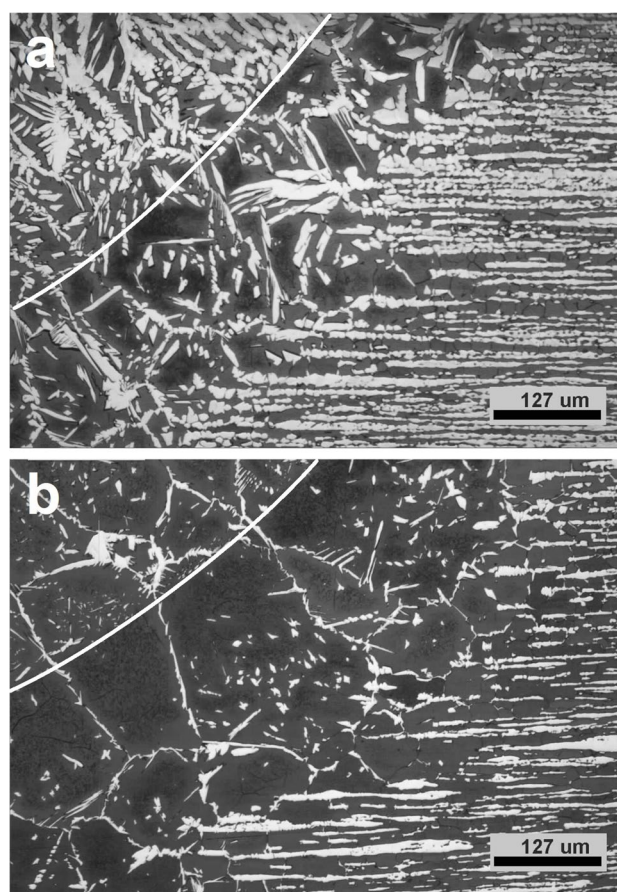

Fig. 10 Fusion line in **a** 4 mm UNS S32101 (Ar + 2% N$_2$) and **b** 5 mm UNS S32304 (Ar + 2% N$_2$)

welding and databases are continuously updated. New and improved simulation approaches are also of importance.

4 Implications

Most welding engineers out on the field do not have access to advanced thermodynamic simulation tools and are more likely to use constitution diagrams. The WRC'92 diagram is currently the most common and accurate prediction tool available [94, 95]. As seen in the calculations presented in Table 1, the prediction for the lean duplex alloys UNS S32101 and UNS S32304 would exceed 100 FN. Figure 9 shows a Fe–Ni–Cr pseudo-binary phase diagram, where the calculated average $(Cr/Ni)_{eq}$ ratio for each alloy has been indicated. This implies that the fully ferritic region would be almost equal for UNS S32101 and UNS S32304. Contrary, it was apparent in this work that there were large variations between these two materials. UNS S32101 was considerably more resistant to ferritization than UNS S32304, with a narrower HT-HAZ containing more austenite, Fig. 10. In UNS S32101, the nickel content has been reduced through a combination of nitrogen alloying and

increased manganese content; 5 wt.-% as compared to 0.7–1.5 wt.-% in the other duplex stainless steels [96]. Manganese is used to increases the solubility of nitrogen, which becomes critical for austenite formation as the nickel content is low [97]. It is possible that this alloying concept would require an adaption of the WRC'92 diagram to include manganese in the Ni_{eq}. As of today, manganese is not included as it is considered neutral with respect to promoting ferrite or austenite during solidification [98]. For the alloy UNS S32101, manganese has been shown to be concentrated in the austenite in the base material and interdendritically in welds solidifying ferritically [53].

In contrast, the Thermo-Calc simulations assuming equilibrium conditions suggested a decrease in the fully ferritic range in the order of UNS S32304 → UNS S32205 → UNS S32750 ≈ UNS S32101. This trend was supported by the actual measurements in the bead-on-plate welds. Although this work could not confirm the absolute ferrite and austenite solvus temperatures, it highlights the valuable insights that can be derived from calculated equilibrium phase diagrams. It is essential to note that welds deviate from equilibrium conditions, and the cooling rate can vary with different methods and material thicknesses. Using DICTRA, the influence of a given cooling rate on microstructure development could be simulated taking the diffusion of especially nitrogen into consideration. The results indicated an increased austenite reformation ability in the order of UNS S32304 → UNS S32205 → UNS S32750 → UNS S32101. In the actual welds, however, no significant difference was observed between UNS S32101 and UNS S32750. Furthermore, the impact of the cooling rate was notably underestimated for all alloys compared to previous observations in thermo-mechanical simulations. Although DICTRA supported the positive effect of nitrogen on the austenite formation and cooling rate, the precision was insufficient as compared to actual measurements of the welds in this study, and the values obtained with the version MOBEFE7 cannot be used to replace actual testing.

The HT-HAZ width was not affected by the choice of shielding gas, but it decreased with the material thickness and nitrogen content. It was often challenging to locate the fusion line, especially when the difference between the HT-HAZ and the weld metal was small. When welding UNS S32101 and UNS S32750 with $Ar + 2\% N_2$ as shielding gas, approximately equal amounts of ferrite were measured in the weld metal and HT-HAZ. On the contrary, the use of Ar lead to nitrogen loss from the weld metal followed by less austenite formation than in the HT-HAZ making it easier to distinguish these two regions and locate the fusion line. With UNS S32304 and to some extent also UNS S32205, the ferrite content was similar in the weld metal and HT-HAZ when using Ar, while additions of nitrogen to the shielding gas promoted formation of significantly more austenite in the weld metal.

In thermo-mechanical simulations, where the entire thickness is subjected to uniform heating, the ferrite content shows a clear relation with the base metal nitrogen content for all cooling rates, Fig. 6a. This type of testing is efficient for fundamental research as larger samples with uniform microstructure can be created and investigated. In real welds, the HT-HAZ is much narrower, which complicates actual testing. It should be noted, however, that the peak temperature and the cooling rate obtained in the Gleeble® may deviate from the conditions in an actual weld. For the bead-on-plate welds here, the partial heating of the material led to considerable cooling rates. This caused somewhat higher ferrite contents than what has been observed in the HT-HAZ after thermo-mechanical simulation. While the bead-on-plate welding can be used for ranking of materials for research purposes, it does not represent the real welding conditions and the measurements cannot be used for qualification of welds. The material thickness of 3–5 mm in this work would require joint preparation and additions of filler metal.

5 Conclusions

GTAW was conducted bead-on-plate for the duplex alloys UNS S32101, UNS S32304, UNS S32205 and UNS S32750 of 3-, 4- and 5-mm thickness with an arc energy of 0.4 kJ/mm and either Ar or $Ar + 2\% N_2$ as shielding gas. Measurements of weld shape, grain size and ferrite content in the HT-HAZ of the welds were compared with values reported for real welds and thermo-mechanical Gleeble® simulations from existing literature. The temperatures at which different phases form were estimated thermodynamically using Thermo-Calc and DICTRA. The following conclusions could be drawn:

1. The ferrite content in the HT-HAZ of the welds performed bead-on-plate was 69–82 vol.-% for UNS S32101, 89–92 vol.-% for UNS S32304, 80–91 vol.-% for UNS S32205 and 65–82 vol.-% for UNS S32750.
2. None of the welds passed the 35–65 vol.-% weld metal ferrite content limit often set by the industry, and only 3 mm UNS S32750 performed with $Ar + 2\% N_2$ as shielding gas was within 30–70 vol.-% in both the weld metal and HAZ.
3. Nitrogen additions to the shielding gas increased the weld metal austenite formation as compared to Ar but had limited effect on the HAZ.
4. The width of the HT-HAZ decreased with the base metal nitrogen content and material thickness, while the ferrite fraction decreased with the nitrogen content but without a clear relation with the material thickness.
5. Bead-on-plate welding does not reflect the real welding conditions and the cooling rate becomes high due to the

shallow penetration. Both proper joint preparation and use of over-alloyed filler metal would be necessary to pass the most stringent requirements in the weld metal.

6. The WRC'92 diagram could not be used to rank the alloys in this work. The calculated ferrite content exceeded 100 FN for both UNS S32101 and UNS S32304. Manganese is not accounted for in the Ni_{eq} formula, but increases the solubility of nitrogen and thus has a great influence on the austenite formation in UNS S32101.

7. Thermo-Calc simulations assuming equilibrium conditions confirmed that the austenite formation starts earlier for alloys with higher nitrogen content. The fully ferritic range calculated with Thermo-Calc decreased in the order UNS S32304 → UNS S32205 → UNS S32750 ≈ UNS S32101, which was in agreement with actual measurements of welded samples.

8. Calculations using DICTRA supported the positive influence of nitrogen on austenite formation, but overestimated the values at high nitrogen contents and underestimated the effect of cooling rate.

Declarations

Conflicts of interest The authors declare no conflicts of interest.

Open access Provided by University West.

References

1. EN ISO 15156-3 (2020) Petroleum and natural gas industries – Materials for use in H$_2$S-containing environments in oil and gas protection. Part 3: Cracking-resistant CRAs (corrosion resistant alloys) and other alloys. European Committee for Standardization, Brussels, Belgium, 80pp.

2. Gunn RN (1997) Duplex stainless steels: microstructure, properties and applications. Woodhead Publishing Ltd, Cambridge, pp 216

3. Karlsson L (2000) Welding of stainless steels. Duplex and super-duplex steels. Weld Int 14(12):5–11. https://doi.org/10.1080/09507110009549131

4. Berglund G, Wilhelmsson P (1989) Fabrication and practical experience of duplex stainless steels. Mater Des 10(1):23–28. https://doi.org/10.1016/0261-3069(89)90031-9

5. Knyazeva M, Pohl M (2013) Duplex steels: Part I: Genesis, formation, structure. Metallogr Microstruct Anal 2(4):113–121. https://doi.org/10.1007/s13632-013-0066-8

6. Omura T, Kushida T, Kudo T, Hayashi T, Matsuhiro Y, Hikida T (1997) Effect of nitrogen distribution on pitting corrosion resistance in high power laser welded duplex stainless steels. Tetsu-to-Hagane 83(9):575–580. https://doi.org/10.2355/tetsutohagane1955.83.9_575

7. Zhang Z, Jing H, Xu L, Han Y, Zhao L (2017) Influence of microstructure and elemental partitioning on pitting corrosion resistance of duplex stainless steel welding joints. Corros Sci 394:194–210. https://doi.org/10.1016/j.apsusc.2016.10.047

8. Liao J (2001) Nitride precipitation in weld HAZs of a duplex stainless steel. ISIJ Int 41(5):460–467. https://doi.org/10.2355/isijinternational.41.460

9. Chen TH, Yang JR (2002) Microstructural characterization of simulated heat affected zone in a nitrogen-containing 2205 duplex stainless steel. Mater Sci Eng A338(1–2):166–181. https://doi.org/10.1016/S0921-5093(02)00065-5

10. Kokawa H, Tsory E, North TH (1995) Nitride precipitation in duplex stainless steel weld metal. ISIJ Int 35(10):1277–1283. https://doi.org/10.2355/isijinternational.35.1277

11. Kokawa H, Umeda S, Kuwana T (1994) Effects of nitrogen on tensile properties of duplex stainless steel weld metal. Weld Int 8(6):531–537. https://doi.org/10.1080/09507119409548630

12. Hu Y, Shi Y-H, Shen X-Q, Wang Z-M (2017) Microstructure, pitting corrosion resistance and impact toughness of duplex stainless steel underwater dry hyperbaric flux-cored arc welds. Materials 10(1443):18. https://doi.org/10.3390/ma10121443

13. Jing H, Xu L, Han Y, Zhao L, Zhou C (2017) Effects of nitrogen in shielding gas on microstructure evolution and localized corrosion behavior of duplex stainless steel welding joint. Appl Surf Sci 404(5):110–128. https://doi.org/10.1016/J.APSUSC.2017.01.252

14. Liou H-L, Hsieh R-I, Tsai W-T (2002) Microstructure and pitting corrosion in simulated heat-affected zones of duplex stainless steels. Mater Chem Phys 74(1):33–42. https://doi.org/10.1016/S0254-0584(01)00409-6

15. Han Y, Zhang Y, Jing H, Gao Z, Xu L, Zhang Z, Zhao L (2020) Microstructure and corrosion studies on different zones of super duplex stainless steel UNS S32750 weldment. Front Mater 7(11):251–15. https://doi.org/10.3389/fmats.2020.00251

16. Ferreira PJ, Hertzman S (1991) δ-Ferrite grain growth in simulated high temperature HAZ of three duplex stainless steels. Proc Duplex Stainless Steels '91 Beaune, France, Les editions de physique 2:959–966

17. Corolleur A, Fanica A, Passot G (2015) Ferrite content in the heat affected zone of duplex stainless steels. BHM 160(9):413–418. https://doi.org/10.1007/s00501-015-0408-8

18. Yang Y, Wang Z, Tan H, Hong J, Jiang Y, Jiang L, Li J (2012) Effect of a brief post-weld heat treatment on the microstructure evolution and pitting corrosion of laser beam welded UNS S31803 duplex stainless steel. Corros Sci 65(8):472–470. https://doi.org/10.1016/j.corsci.2012.08.054

19. Liljas M (1995) The welding metallurgy of duplex stainless steels. Proc Duplex Stainless Steels '94, Glasgow, Scotland, TWI 2(Paper KV):15

20. Ogawa T, Koseki T (1989) Effect of composition profiles on metallurgy and corrosion behavior of duplex stainless steel weld metals. Weld J Res Suppl 68(5):181s–191s. http://files.aws.org/wj/supplement/WJgamma1989_05_s181.pdf

21. Kotecki DJ (2013) Landmark events in the welding of stainless steels. Adv Mater Res 794(9):257–273. https://doi.org/10.4028/www.scientific.net/AMR.794.257

22. Cao H-L, Hertzman S (1991) The relationship between impact properties and welding simulated microstructures in three duplex stainless steels. Proc Duplex Stainless Steels '91 Beaune, France, Les editions de physique 1:363–324

23. Kotecki DJ (1986) Ferrite control in duplex stainless steel weld metal. Weld J Res Suppl 65(10):273s–278s

24. Hosseini VA, Wessman S, Hurtig K, Karlsson L (2016) Nitrogen loss and effects on microstructure in multipass TIG welding of a super duplex stainless steel. Mater Des 98(5):88–97. https://doi.org/10.1016/j.matdes.2016.03.011

25. Westin EM, Johansson MM, Pettersson RFA (2013) Effect of nitrogen-containing shielding and backing gas on the pitting corrosion resistance of welded lean duplex stainless steel LDX 2101® (EN 1.4162, UNS S32101). Weld World 57(7):467–476. https://doi.org/10.1007/s40194-013-0046-2

26. Migiakis K, Papadimitriou GD (2009) Effect of nitrogen and nickel on the microstructure and mechanical properties of plasma welded UNS S32760 super-duplex stainless steels. J Mater Sci 44(12):6372–6383. https://doi.org/10.1007/s10853-009-3878-9

27. Hertzman S (2001) The influence of nitrogen on microstructure and properties of highly alloyed stainless steel welds. ISIJ Int 41:580–589. https://doi.org/10.2355/isijinternational.41.580

28. Westin EM, Johansson MM, Bylund L-Å, Pettersson RFA (2014) Effect on microstructure and properties of super duplex stainless steel welds when using backing gas containing nitrogen and hydrogen. Weld World 58(5/6):347–354. https://doi.org/10.1007/s40194-014-0120-4

29. Westin EM, Serrander D (2012) Experience in welding stainless steels for water heater applications. Weld World 56(5/6):14–28. https://doi.org/10.1007/BF03321346

30. Valiente Bermejo MA, Thalavai PK, Axelsson B, Harati E, Kisielewicz A, Karlsson L (2021) Microstructure of laser metal deposited duplex stainless steel: Influence of shielding gas and heat treatment. Weld World 65(3):525–541. https://doi.org/10.1007/s40194-020-01036-5

31. Varbai B, Adonyi Y, Baumer R, Pickle T, Dobránszky J, Májlinger K (2019) Weldability of duplex stainless steels – Thermal cycle and nitrogen effects. Weld J Res Suppl 98(3):78s–87s. https://doi.org/10.29391/2019.98.006

32. Hosseini VA, Karlsson L (2019) Physical and kinetic simulation of nitrogen loss in high temperature heat affected zone of duplex stainless steels. Materialia 6(6):762–775. https://doi.org/10.1016/j.mtla.2019.100325

33. Westin EM, Westerberg LG (2023) Evaluation of methods for simulation of heat-affected zones in duplex stainless steels. In press, Weld World. https://doi.org/10.1007/s40194-024-01698-5

34. Lippold JC, Kotecki DJ (2005) Welding metallurgy and weldability of stainless steels. John Wiley & Sons, Inc., New Jersey, 376pp. ISBN: 978–0–471–47379–4

35. Tsuge H, Tarutani Y, Kudo T (1988) The effect of nitrogen on the localized corrosion resistance of duplex stainless steel simulated weldments. Corrosion 44(5):305–314. https://doi.org/10.5006/1.3583942

36. Hertzman S, Ferreira PJ, Brolund B (1997) An experimental and theoretical study of heat-affected zone austenite reformation in three duplex stainless steels. Metall Mater Trans A 28(2):277–285. https://doi.org/10.1007/s11661-997-0130-6

37. Lindblom BES, Lundqvist B, Hannerz NE (1991) Grain growth in HAZ of duplex stainless steels. Scand J Metallurgy 20(5):305–315

38. Hsieh R-I, Liou H-Y, Pan Y-T (2001) Effects of cooling time and alloying elements on the microstructure of the Gleeble-simulated heat-affected zone of 22% Cr duplex stainless steels. J Mater Eng Perform 10(10):526–536. https://doi.org/10.1361/105994901770344665

39. Westin EM, Brolund B, Hertzman S (2008) Weldability aspects of a newly developed duplex stainless steel LDX 2101. Steel Res Int 79(6):473–481. https://doi.org/10.1002/srin.200806155

40. Guo Y, Sun T, Hu J, Jiang Y, Jiang L, Li J (2016) Microstructure evolution and pitting corrosion resistance of the Gleeble-simulated heat-affected zone of a newly developed lean duplex stainless steel. J Alloys Compd 658(2):1031–1040. https://doi.org/10.1016/j.jallcom.2015.10.218

41. Varbai B, Pickle T, Májlinger K (2019) Effect of heat input and role of nitrogen on the phase evolution of 2205 duplex stainless steel weldment. Int J Press Vessels Pips 176(9):103952. https://doi.org/10.1016/j.ijpvp.2019.103952

42. Hsieh R-I, Liou H-Y, Pan Y-T (1999) Weldability of 22% Cr duplex stainless steels. China Steel Tech Rep 13:14–26

43. Yang Y, Yan B, Li J, Wang J (2011) The effect of large heat input on the microstructure and corrosion behaviour of simulated heat affected zone in 2205 duplex stainless steel. Corros Sci 53(11):3756–3763. https://doi.org/10.1016/j.corsci.2011.07.022

44. Komenda J, Sandström R (1995) Quantitative characterisation of weld simulated structures in duplex stainless steel SAF 2205. Acta Stereol 14(1):29–34. http://popups.uliege.be/0351-580x/index.php?id=663&file=1&pid=662 accessed on 2021–11–09

45. Kim D-C, Ogura T, Yamashita S, Oikawa Y, Saida K (2020) Computer prediction of α/γ phase fraction in multi-pass weld of duplex stainless steel and microstructural improvement welding process. Mater Des 196(109154)10. https://doi.org/10.1016/j.matdes.2020.109154

46. Yamashita S, Ike K, Yamasaki K, Wei F-G, Wang K, Ogura T, Saida K (2022) Relationship between ferrite-austenite phase transformation and precipitation behavior of sigma phase in super duplex stainless steel weldment. Weld World 66(2):351–362. https://doi.org/10.1007/s40194-021-01239-4

47. Lippold JC, Al-Rumaih AM (1997) Toughness and pitting corrosion of duplex stainless steel weld heat-affected zone microstructures containing secondary austenite. Proc Duplex Stainless Steels '97 KCI Publishing, Paper D97–115:1005–1009

48. Pettersson N, Wessman S, Hertzman S, Studer A (2017) High-temperature phase equilibria of duplex stainless steels assessed with a novel in-situ neutron scattering approach. Metall Mater Trans A 48(4):1562–1571. https://doi.org/10.1007/s11661-016-3953-1

49. Ramirez AJ, Brandi SD, Lippold JC (2004) Secondary austenite and chromium nitride precipitation in simulated heat affected zones of duplex stainless steels. Sci Tech Weld Joi 9(4):301–313. https://doi.org/10.1179/136217104225021715

50. Palmer TA, Elmer JW, Babu SS (2004) Observations of ferrite/austenite transformations in the heat affected zone of 2205 duplex stainless steel spot welds using time resolved X-ray diffraction. Mater Sci Eng A 374(1–2):307–321. https://doi.org/10.1016/j.msea.2004.03.037

51. Komizo Y, Ogawa K, Azuma S (1991) HAZ embrittlement in high Cr-Mo duplex stainless steel and the effects of Ni and N. Weld Int 5(4):277–282. https://doi.org/10.1080/09507119109446735

52. Brandi SD (2003) Some aspects of weldability and jointability of duplex stainless steels. Mater Sci Forum 426–432(8):4063–4068. https://doi.org/10.4028/www.scientific.net/MSF.426-432.4063

53. Westin EM, Hertzman S (2014) Element distribution in lean duplex stainless steel welds. Weld World 58(3):143–160. https://doi.org/10.1007/s40194-013-0108-5

54. Sundman B, Jansson B, Andersson J-O (1985) The Thermo-Calc Databank System. Calphad 6(2):153–190. https://doi.org/10.1016/0364-5916(85)90021-5

55. Johansson C, Lind M (2015) Evaluation of the η (Eta) nitride with three laboratory melts. Diploma Work, KTH Royal University of Technology, Stockholm, Sweden, 153pp. https://www.diva-portal.org/smash/get/diva2:865850/FULLTEXT01.pdf

56. Morales EV, Pozo JA, Olaya L, Kassab E, Ponciano JAC, Ghavami K, Bott IS (2019) Remarks on the evolution and performance of the different austenite morphologies at the simulated HAZs of a 2205 duplex stainless steel. J Mater Res Technol 8(5):3936–3949. https://doi.org/10.1016/j.jmrt.2019.07.002

57. Jargelius-Pettersson R, Hertzman S, Szakalos P, Ferreira PJ (1994) The influence of microstructure in pitting corrosion in autogenous TIG duplex stainless steel welds. Proc. Duplex Stainless Steels '94, Glasgow, Scotland, TWI, 461–472

58. Watanabe K, Masuda K (1995) Effects of residuals and micro-alloying elements on welding of stainless steels. Part 1: Effects of weld pool behavior by GTAW. IIW Doc. IX-H-348–95. International Institute of Welding, 18pp.

59. Wang K, Jiao X, Zhu J, Shao C, Li C (2022) Effect of nitrogen protection on weld metal microstructure and intergranular behavior of S32101 duplex stainless steel 15m water depth hyperbaric laser underwater welding. Adv Mech Eng 14(1):1–12. https://doi.org/10.1177/16878140211072943

60. Holländer Pettersson N, Lindell D, Lindberg F, Borgenstam A (2019) Formation of chromium nitride and intragranular austenite in a super duplex stainless steel. Metall Mater Trans A 50(12):5594–5601. https://doi.org/10.1007/s11661-019-05489-2

61. Valiente Bermejo MA, Hurtig K, Eyzop D, Karlsson L (2019) A new approach to the study of multi-pass welds – microstructure and properties of welded 20-mm-thick superduplex stainless steel. Appl Sci 9(1050):18. https://doi.org/10.3390/app9061050

62. Yasuda K, Tamaki K, Nakano S, Kobayashi K, Nishiyama N (1986) Metallurgical characteristics of weld metals and corrosion performance of girth weld joints of duplex stainless steel pipes. Proc Duplex Stainless Steels '86 The Hague, The Netherlands, NIL, Paper 24:201–212

63. Hertzman S, Roberts W, Lindenmo M (1986) Microstructure and properties of nitrogen alloyed stainless steel after welding treatments. Proc Duplex Stainless Steels ´86 The Hauge, The Netherlands, NIL, Paper 30:257–263

64. Sridhar N, Kolts J (1987) Effects of nitrogen on the selective dissolution of a duplex stainless steel. Corrosion 43(11):646–651. https://doi.org/10.5006/1.3583843

65. Picke T, Henry N, Morriss P, Tennis L, Wagner D, Baumer RE (2019) Root pass microstructure in super duplex stainless steel multipass welds. Weld J 98(5):123s–134s. https://doi.org/10.29391/2019.98.010

66. Baghdadchi A, Hosseini VA, Valiente Bermejo MA, Axelsson B, Harati E, Högström M, Karlsson L (2022) Wire laser metal deposition of 22% Cr duplex stainless steel: as-deposited and heat-treated microstructure and mechanical properties. J Mater Sci 57(1):9556–9575. https://doi.org/10.1007/s10853-022-06878-6

67. ASTM G48 (2016) Standard test methods for pitting and crevice corrosion resistance of stainless steels and related alloys by use of ferric chloride solution. ASTM International. West Conshohocken, PA, USA, p 11

68. ASTM A923 (2014) Standard test methods for detecting detrimental intermetallic phase in duplex austenitic/ferritic stainless steels. ASTM International. West Conshohocken, PA, USA, p 9

69. ISO 17781 (2017) Petroleum, petrochemical and natural gas industries – Test methods for quality control of microstructure of ferritic/austenitic (duplex) stainless steels. European Committee for Standardization. Brussels. Belgium, p 34

70. Lundqvist B, Norberg P, Olsson K (1986) Influence of different welding conditions on mechanical properties and corrosion resistance of Sandvik SAF 2205 (UNS S31803). Proc Duplex Stainless Steels '86, The Hague, NL, NIL, Paper 10:16–29

71. Sicupira DC, Cardoso Junior R, Bracarense AQ, Frankel GS, Lins VFC (2017) Cyclic polarization study of thick welded joints of lean duplex stainless steel for application in biodiesel industry. Mater Res 20(1):161–167. https://doi.org/10.1590/1980-5373-MR-2016-0370

72. Yan HT, Xin SS, Yang Y, Yang S, Li MC (2019) Electrochemical corrosion behavior of 2205 duplex stainless steel welds in chloride solutions. Int J Electrochem Sci 14(1):1423–1433. https://doi.org/10.20964/2019.02.54

73. Moreira da Silveira D (2013) Avaliação da resistência à corrosão de juntas soldadas de aço inoxidável lean duplex UNS S32304 usando espectroscopia de impedância eletroquímica. PhD thesis, Universidade Federal de Minas Gerais, Belo Horizonte, 126pp. https://repositorio.ufmg.br/bitstream/1843/BUBD-9FVEXJ/1/tese_corrigida.pdf

74. Tan H, Wang Z, Jiang Y, Han D, Hong J, Chen L, Jiang L, Li J (2011) Annealing temperature effect on the pitting corrosion resistance of plasma arc welded joints of duplex stainless steel UNS S32304 in 1.0M NaCl. Corros Sci 53(6):2191–2200. https://doi.org/10.1016/j.corsci.2011.02.041

75. Júnior RC, Esteves L, Santos NF, Oliveira IR, Mendes DS, Lins VFC, Modenesi PJ (2019) J Mater Eng Perform 28(3):1969–1976.https://doi.org/10.1007/s11665-019-03967-7

76. Chen L, Tan H, Wang Z, Li J, Jiang Y (2015) Influence of cooling rate on microstructure evolution and pitting corrosion resistance in the simulated heat-affected zone of 2304 duplex stainless steels. Corros Sci 58(5):168–174. https://doi.org/10.1016/j.corsci.2012.01.018

77. ASTM G150 (2018) Standard test method for electrochemical critical pitting temperature testing of stainless steels and related alloys. ASTM Int., West Conshohocken, PA, USA, p 28

78. Qvarfort R (1988) New electrochemical cell for pitting corrosion testing. Corros Sci 28(2):135–140. https://doi.org/10.1016/0010-938X(88)90090-X

79. Qvarfort R (1989) Critical pitting temperature measurements of stainless steels with an improved electrochemical method. Corros Sci 29(8):987–993. https://doi.org/10.1016/0010-938X(89)90088-7

80. Geng S, Sun J, Guo L, Wang H (2015) Evolution of microstructure and corrosion behavior in 2205 duplex stainless steel GTA-welding joint. J Manuf Process 19(8):32–37. https://doi.org/10.1016/j.jmapro.2015.03.009

81. Westin EM (2010) Pitting corrosion resistance of GTA welded lean duplex stainless steel. Weld World 54(11/12):R308-321. https://doi.org/10.1007/BF03266745

82. Valiente Bermejo MA, Eyzop D, Hurtig K, Karlsson L (2021) Welding of large thickness super duplex stainless steel: Microstructure and properties. Metals 11(1184):22. https://doi.org/10.3390/met11081184

83. Turner S, Robinson FPA (1989) The effect of the surface oxides produced during welding on the corrosion resistance of stainless steels. Corrosion 45(9):710–716. https://doi.org/10.5006/1.3585023

84. Rastogi PK, Shah BK, Sinha AK, Kulkarni PG (1994) Effect of oxide film on pitting susceptibility of 304 austenitic stainless steel. British Corros J 29(1):78–80. https://doi.org/10.1179/000705994798267953

85. Azuma S, Miyuki H, Murayama J, Kudo T (1990) Effect of weld scale on corrosion resistance of stainless steels. Corros Eng 39(11):603–609. https://doi.org/10.3323/jcorr1974.39.11_603

86. Pettersson RFA, Flyg J (2005) Influence of weld oxides on the corrosion of 316L stainless steel. Proc Eurocorr 2005, Lisbon, Portugal, Rolo&Filhos Lda, Paper 644:9

87. von Moltke T, Pistorius PC, Sandenbergh RF (1992) The influence of heat-tinted surface layers on the corrosion resistance of stainless steels. Proc First Int Chromium Steel Alloys Congress, INFACOM 6 Chromium Steel Alloys, Cape Town, South Africa, Johannesburg, SAIMM 2:185–195

88. Fuertes N, Bengtsson R, Pettersson R, Rohwerder, (2016) Use of SVET to evaluate corrosion resistance of heat tints on stainless steel welded joints and effect of different post-weld cleaning treatments. Mater Corros 68(1):7–19. https://doi.org/10.1002/maco.201609048

89. Westin EM, Olsson C-OA, Hertzman S (2008) Weld oxide formation on lean duplex stainless steel. Corros Sci 50(9):2620–2634. https://doi.org/10.1016/j.corsci.2008.06.024

90. Rodriguez BR, Miranda A, Gonzalez D, Rolando Praga R, Hurtado E (2020) Maintenance of the austenite/ferrite ratio balance in GTAW DSS joints through process parameters optimization. Materials 13(3):780–796. https://doi.org/10.3390/ma13030780

91. Soares da Fonseca G, Rodrigues Barbosa LO, Alves Ferreira E, Xavier CR, Adilson de Castro J (2017) Microstructural, mechanical, and electrochemical analysis of duplex and super-duplex stainless steels welded with the autogenous TIG process using different heat input. Metals 358(7):21. https://doi.org/10.3390/met7120538

92. Westin EM, Johansson MM, Bylund L-Å, Pettersson RFA (2014) Effect on microstructure and properties of super duplex stainless steel welds when using backing gas containing nitrogen and hydrogen. Weld World 58:347–354. https://doi.org/10.1007/s40194-014-0120-4l

93. Gupta A, Kumar A, Baskaran T, Arya SB, Khatirkar RK (2018) Effect of heat input on microstructure and corrosion behavior of duplex stainless steel shielded metal arc welds. Trans Indian Inst Met 71(2):1595–1606. https://doi.org/10.1007/s12666-018-1294-z

94. Kotecki DJ, Siewert TA (1992) WRC-1992 constitution diagram for stainless steel weld metals – a modification of the WRC 1988 diagram. Weld J 71(5):171s–178s

95. ISO/DTR 22824 (2023) Welding consumables – Predicted and measured FN in specifications – A position statement of the experts of IIW Commissions II and IX. Editor Dr. Damian Kotecki. 2nd Edition. In: preparation. European Committee for Standardization, Brussels, Belgium, p 38

96. Liljas M, Johansson P, Liu H-P, Olsson C-OA (2016) Development of a lean duplex stainless steel. Steel Res Int 79(6):466–473. https://doi.org/10.1002/srin.200806154

97. Pitkälä J, Holappa L, Jokilaakso A (2022) A study of the effect of alloying elements and temperature on nitrogen solubility in industrial stainless steelmaking. Metall Mater Trans B 53(5):2364–2376. https://doi.org/10.1007/s11663-022-02534-1

98. Szumachowski ER, Kotecki DJ (1984) Effect of manganese on stainless steel weld metal ferrite. Weld J 63(5):156s–161s